EISCAT_3D
Options for the active element

Gudmund Wannberg

IRF Technical Report 051
February 2009

ISSN 0284-1738

INSTITUTET FÖR RYMDFYSIK

Swedish Institute of Space Physics

Kiruna, Sweden

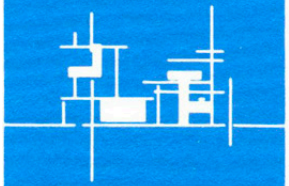

Institutet för rymdfysik
Swedish Institute of Space Physics

EISCAT_3D DELIVERABLE 3.2:

OPTIONS FOR THE ACTIVE ELEMENT

Gudmund Wannberg
Swedish Institute of Space Physics
Box 812
SE-98128 Kiruna
Sweden
ugw@irf.se

2009-02-02

Table of Contents

List of Tables

List of Figures

Executive Summary

- As specified already in the EISCAT_3D Performance Specification Document PSD, only a full-fledged phased array system can reach or approach the active element performance demanded by the scientific user community. This is therefore the system of choice.

- The active element array shall be a filled circular aperture with the array elements laid out on an equilateral triangular grid. An element-element distance of 0.7 λ will provide essentially grating-lobe free performance out to 40^{o} zenith angle.

- The individual array element will comprise a radiator, a dual 300+300 watt linear RF power amplifier, a high performance direct-digitising receiver, a digital signal processing system and support electronics. The preferred radiator is a crossed Yagi antenna with a minimum directivity of about 7 dBi, e.g. the so-called "Renkwitz Yagi".

- The array will be physically subdivided into hexagonal groups of 49 elements. For practical reasons, all electronics for the group will be housed in a common equipment container and the radiators connected to the container by low-loss coax cable.

- The target is a 16000-element, 120-m diameter array. This will have a half-power beamwidth of $\approx 0.75^{o}$, i.e. comparable to that of the EISCAT UHF. Its power-aperture product will be $\approx$ 100 GW m^2, i.e. about one order of magnitude greater than that of the EISCAT VHF when operated in single-beam, dual klystron mode (Mode 1).

- To get started with limited funding, already a 5000-element, 70-m diameter array would exceed the performance of the current VHF system, providing a 1.3^{o} half-power beam-width, a power-aperture product of $\approx$ 10 GW m^2, and full steerability. This array could then be expanded as additional funding became available. Provisions for expansion should be built in from the beginning.

- In either case, a basic set of receive-only outlier arrays for interferometry should be put in place from the start to meet the horizontal resolution performance requirement.

- The extreme joint time/height resolution requirements laid down in PSD Section 2.12 are unrealistic; even a 36000-element array configuration would fail to meet them at all altitudes by a factor of 25…350!

- Relaxing the height resolution by a factor of 4…10 (from 100 m to 1 km at 150-km altitude and from 1 km to 4 km at 300-km altitude), will put the 16000-element array in a position to meet the PSD time resolution requirements.

- Agreement on whether incoherent-scatter altitude resolutions better than 1 km are really scientifically meaningful and required at altitudes above 150 km must be reached before the 3D project proceeds to the RFQ phase.

Introduction

The task of Work Package 3, "Options for the active element", aka WP3, is defined as a high-level study of different system architectures for the EISCAT_3D active ("core") element and the identification of a preferred core site architecture.

The original objectives included an unprejudiced investigation of a range of hardware configurations; from a conventional high power transmitter feeding several reflector antennas, through a partially distributed system, to a full-fledged phased array, and an investigation of how well (if at all) the different configurations would meet the performance requirements laid down in Work Package 2. In this context, it was also planned to investigate the feasibility and suitability of re-using part of the existing EISCAT VHF installation as a component part of a future 3D system. This is reflected in the wording describing the WP3 objectives on page 7 of the EISCAT_3D Project Plan (Annex 1 to the EU FP6 contract) [1]:

"A major part of the cost of the new facility will be invested in the production of the high-power transmission capability. The relative benefits of different approaches, ranging from a multi-component transmitter / multi-feed conventional antenna design to a full phased array with the transmitter integral with, and distributed across, the antenna, will be evaluated as part of this Work Package and used to identify the optimum solution in terms of scientific return, performance, ease of manufacture and cost."

This prudent plan was overtaken by events already before WP3 had started. Once the results of the WP2 Questionnaire had been compiled, it was evident that the performance expected by the scientific user community could in fact only be delivered by a full phased array system, thus rendering the spending of any effort on investigating other options pointless. Accordingly, WP3 was re-focussed onto studying how to best map the 3D core site performance requirements, as based on user input and summarised in the EISCAT_3D Performance Specification Document, aka known as the PSD [2], onto a realisable, practical and reliable phased array. This demanded considerably more time and effort than originally assigned to this WP, but as a thorough understanding of the array design boundary conditions and tradeoffs was clearly fundamental to a number of other Work Packages, notably WP6, the extra effort was regarded as essential and absorbed.

The present report summarises the results from Work Package 3 in eight sections:

- In Section 1, the EISCAT_3D Performance Specification Document [2] is revisited and core array design-driver performance requirements are identified,

- In Section 2, some important results and conclusions from the RF power amplifier study conducted in WP6 are highlighted and a target number for the RF power level per element radiator is given,

- Section 3 begins by some basic array theory. First-order relationships connecting the pattern, gain, grating-lobe behaviour and number of array elements of a 2-d phased array to array size and element-element distance are derived. Two regular array geometries (square and equilateral triangular) are considered, the triangular one is identified as superior, and a range of different size arrays are evaluated with regard to gain and beam-width. It is shown that the transverse spatial resolution requirement cannot be met by a reasonably-sized filled array but only by interferometric means,

- Section 4 considers the element radiator design problem from the electrical and practical points of view. Reference is made to the excellent NEC analysis of a range of short Yagis and the numerical simulations of the pattern and gain of several very large arrays contained in Mr. Renkwitz' M. Sc. Eng. thesis. Results from impedance measurements on a full-scale prototype of the X Yagi proposed by Mr. Renkwitz as a suitable candidate for the element radiator are presented and compared to the NEC results,

- In Section 5, the monostatic incoherent-scatter radar equation is used to analyse the PSD incoherent-scatter time resolution requirements in terms of the required radar power-aperture product and the attendant array size,

- Section 6 addresses some practical construction aspects, including how to strike an optimal trade-off between array sub-group size and cable-attenuation induced loss of performance.

- Section 7 discusses how to implement the core array receiving function,

- Conclusions and recommendations are summarised in Section 8.

1. Performance requirements governing the Active Element design

The overall technical characteristics and performance requirements relevant to the design of the Active Element are defined in the following excerpts from the PSD [2]. In the subsequent sections, we investigate how these requirements can be translated into a practically realisable system configuration:

Science Goals

…The design goals mandate improvements in the achievable temporal and spatial resolution (both parallel and perpendicular to the radar line-of-sight) by about an order of magnitude…

Central transmitting/receiving core

This will comprise:

- a phased-array transmit/receive (TX/RX) system with at least one antenna,
- RF signal generation equipment and RF power amplifiers,
- a transmit/receive switching system,
- beam-steering systems for transmission and reception,
- several (4–10) outlier, receive-only phased-array antennas for in-beam interferometry,
- an incoherent-scatter receiver subsystem,
- an interferometry receiver subsystem,
- time and frequency synchronisation equipment,
- digital signal processing equipment,
- built-in test equipment (BITE)

Spatial resolution

The transmitter and antenna parameters will be selected such that, over the multi-static field-of-view: the resolution along the transmitted beam direction(s) can be made better than 100 m at any altitude, the horizontal –3 dB resolution at 100 km altitude is better than 150 m.

Radar field-of-view (FOV)

The beam generated by the central core transmit/receive antenna array will be steerable out to a maximum zenith angle of 40° in all azimuth directions.

Transmitter parameters

Centre frequency: between 220 – 250 MHz, subject to allocation
Peak output power: ≥2 MW
Instantaneous –1 dB power bandwidth: ≥5 MHz
Pulse length: 0.5–2000 μs
Pulse repetition frequency: 0–3000 Hz
Modulation: Arbitrary waveforms, limited only by power bandwidth

Sensor performance in in-beam interferometer mode

In interferometer mode, the sensor will provide horizontal, 2D resolution of better than 20 m at 100 km altitude. To achieve this, the interferometry receiver subsystem together with the main TX/RX antenna and the outlier receiving antenna arrays shall be arranged to provide samples of the target visibility function on ~150 different baselines with lengths ranging from about six wavelengths to more than 750 wavelengths.

Sensor performance in incoherent scatter mode

The parameters of the different subsystems will be chosen such that, for each of the measurement scenarios tabulated below, the radar will generate estimates of incoherently scattered signal power (or equivalently, uncorrected electron density) with statistical accuracies of better than 10 % in the specified integration times:

Altitude [km]	Electron density [m^{-3}]	T_e/T_i	Ion composition	Height resolution [m]	Integration time [seconds]
80	1×10^{8}	1.0		≤100	30
100	3×10^{9}	1.0		100	1
150	1×10^{10}	1.0	50% NO^+, 50% O^+	100	1
300	3×10^{10}	2.0	100% O^+	300	1
800	3×10^{10}	3.0	5% H^+, 95% O^+	1000	10
1500	1×10^{10}	4.0	10% H^+, 90% O^+		60

2. RF power amplifiers

RF signals generation, RF power amplifier design and EI_3D-specific design considerations are the subject and responsibility of WP6. A brief review of the results achieved so far is presented below for the purpose of establishing a baseline power level to be used in the array performance analysis in Section 5.

It has been verified that a straightforward, easily duplicated, wide-bandwidth class-AB amplifier design using the Philips/NXP BLF248 FET can deliver 300 W continuous-carrier power at 225 MHz with good RF and thermal stability. Results from the detailed evaluation and stress testing of a number of these amplifiers, as well as the evaluation of digital signal generation techniques, will soon be published as Deliverable D 6.2 "EISCAT_3D Active Element Subsystem Design Document".

The BLF248 is a mature component, originally designed for use as the active device in analogue VHF TV transmitter power amplifiers [3]. First released in 1997, it is still in full production, but may soon be discontinued as terrestrial TV broadcasting worldwide changes over to digital. However, several semiconductor manufacturers have recently introduced new LDMOS VHF power FETs delivering up to 500 W per device (e.g. the BLF369), so it can be assumed that RF power devices functionally equivalent to, or better than, the BLF248 will continue to be available off-the-shelf at least for the next 3 – 5 years.

In the following analysis, we therefore assume that the RF power required for each element will be generated by two 300-W RF power amplifier modules, similar to the WP6 BLF248-based test bed, for a total of 600 W per element. This is a very practical power level that will allow the use of standard coaxial components throughout, minimise the risk of expensive failures caused by RF arc-overs or burn-throughs and ease the transmit-receive switch performance requirements. A minimum of 3400 element radiators will be required to reach the 2-MW design target peak power level.

Assuming an inter-element distance in the order of 0.7 λ, the array power density will be about 1 kW m^{-2} at λ = 1.25 m, i.e. comparable to the power density at the reflector of the EISCAT VHF parabolic cylinder antenna.

The power amplifiers will be biased for linear class-AB2 operation in order to accommodate future developments in radar coding, including the possible use of combined phase and amplitude modulations, and to permit the introduction of any desired form of aperture tapering. This flexibility will come at the cost of about 10% lower DC-to-RF conversion efficiency than that of an optimised class-E design.

3. The aperture array

In the early stages of the EI_3D study, a mathematically stringent analysis of the characteristics and performance of phased arrays, with special emphasis on the receive-only (WP 4) arrays, was performed [4]. As part of this work, which started from first principles, a comprehensive Matlab code suite for analysing and presenting the radiation pattern of orthogonal grid arrays was developed. This code is expected to be of great value for the detail-level analysis of the planned array that will have to follow in the next stage of the 3D project.

Since the remit of Work Package 3 is primarily to establish the main design features of the active element (the "core") and offer guidelines for its realisation, we have decided to adopt a simplified, practically oriented first-order approach that highlights a number of important design- and cost-driver aspects, rather than following the WP4 analysis in detail. In what follows, system performance requirements such as e.g. array beam-width and time and altitude resolution will be translated into demands on array size and structure, radiator performance, transmitter power, receiver performance and practical arrangements, with sufficient accuracy to enable a follow-on study to immediately proceed to a detail-level analysis.

3.1 Angular resolution / beamwidth vs. aperture size

To first order, the angular resolution of a filled-aperture antenna in the far field is inversely proportional to the physical extent of the aperture as projected onto the beam direction. A circular, uniformly filled and illuminated aperture array of diameter D_A, operating at a wavelength λ with all elements in phase, will thus produce a main beam of half-width α:

$$\alpha \cong 1.22\,\lambda / D_A \tag{3.1}$$

Conversely,

$$D_A \cong 1.22\,\lambda / \alpha \tag{3.2}$$

or, with α_d in degrees:

$$D_A \cong 69.9\,\lambda / \alpha_d \tag{3.3}$$

At the planned EI_3D operating frequency, 235 -236 MHz, λ = 1.270 m, leading to

$$D_A(236MHz) \cong 88.79 / \alpha_d \tag{3.4}$$

In PSD Section 2.5, the required horizontal resolution is specified as:

"The …. antenna parameters will be selected such that, over the multi-static field-of-view, the horizontal –3 dB resolution at 100 km altitude is better than 150 m."

The beam angular resolution α required to meet this requirement is a function of the beam zenith angle θ:

$\alpha \leq$ 150 sin θ / 10^5 = 1.5 · 10^{-3} sin θ radians or 8.6 · 10^{-2} sin θ degrees

Inserting this into (3.4) yields

$$D_A \geq (1.03 \cdot 10^3 / \sin\theta) \text{ m} \tag{3.5}$$

For a vertically pointing beam, this reduces to:

$$D_A \geq 1.03 \cdot 10^3 \text{ m} \tag{3.6}$$

Since constructing a filled 1-km diameter array must be assumed to be out of the question financially (cf. the Square Kilometer Array!) and probably scientifically unjustified for reasons that will be mentioned later, it is clear that an interferometric arrangement must be employed to reach the design target horizontal resolution; this is why provisions for in-beam interferometry are mandated in the PSD. An in-depth analysis of the design issues pertaining to the realisation of the interferometric system can be found in a series of reports published by the Work Package 5 project team [5, 6].

3.2 Array structure, inter-element distances and grating lobes

To keep cost and complexity down insofar as possible, practical aperture array designs tend to reduce the number of elements to the bare minimum consistent with the optical requirements. The element radiators are also often arranged in a regular pattern (e.g. by rows and columns). Here, we demonstrate why equilateral triangular array geometry is considered preferable to square grid geometry in the EISCAT_3D case.

When the element radiators of a circular aperture of diameter D_A are arranged on an orthogonal (square) grid with nearest-neighbour element spacing d_s, n_s elements are required to fill the aperture:

$$n_s \cong \pi/4 (D_A/d_s)^2 = 0.785 \, (D_A/d_s)^2 \tag{3.9}$$

If the elements are instead arranged on an equilateral triangular grid with element spacing d_t, n_t elements will be required:

$$n_t \cong \frac{\pi}{2\sqrt{3}} (D_A/d_t)^2 = 0.91 \, (D_A/d_t)^2 \tag{3.10}$$

The square array structure will therefore require about 16 % fewer elements than an equilateral triangular one, assuming equal element spacing.

At this point, we recall that any phased array employing an inter-element distance $d > 0.5 \, \lambda$ will develop higher-order interference maxima in directions far away from the main lobe as the phase shift between neighbouring array elements is increased beyond some critical value. These so-called *grating lobes* usually render the array unserviceable for its intended purpose. An excellent formal treatment of the grating lobe problem is given in [7, p. 354 and 372-373]. Below, we use a simple approach to get a qualitative understanding of the problem.

Following [8, eq. 2-10] the far-field array factor $E_a(\theta)$ of a one-dimensional (linear) array of N elements with inter-element distance d, set up to generate a main beam at an angle θ_0 off the normal to the array, is

$$E_a(\theta) = \frac{\sin\left[N\frac{\pi d}{\lambda}(\sin\theta - \sin\theta_0)\right]}{\sin\left[\frac{\pi d}{\lambda}(\sin\theta - \sin\theta_0)\right]} \tag{3.11}$$

If, for any θ_0 there exists a θ $\left[-\frac{\pi}{2} \le \theta \le \frac{\pi}{2}, \theta \ne \theta_0\right]$ for which the denominator vanishes, a grating lobe will be excited in the θ direction.

For $\theta_0 < 0$, a first-order grating lobe will thus appear in-line with the array, i.e. at $\theta = \frac{\pi}{2}$, when

$$d = \frac{\lambda}{1 - \sin\theta_0} \tag{3.12}$$

More generally, to keep the array pattern free from grating lobes out to some specified off-normal angle θ_M the inter-element distance d must satisfy

$$d \le d_M = \frac{\lambda}{1 + |\sin\theta_M|} \tag{3.13}$$

This one-dimensional result can be extended to two dimensions and applied to a regular two-dimensional plane array, deployed on the ground with its normal aligned with the vertical. In this case, θ_0 in Equations 3.11 and 3.12 is the zenith angle. The PSD specifies that it must be possible to steer the core array beam out to $\theta_0 = 40^o$ in all azimuths.

d_M in Eq. 3.13 is now a function of the array structure and the azimuth angle φ. Viewing the array edge-on from a point in the far-field, the transverse angular extent of the array shrinks to almost zero and the lines-of-sight to all elements are essentially parallel. If the array elements are arranged as a square grid with inter-element distance d_s (Figure 1a), the effective d_M is

$$d_{M,s} = d_s \max\left(|\cos\varphi|, |\sin\varphi|\right),\ 0 \le \varphi \le 2\pi \tag{3.14}$$

If instead an equilateral triangular grid with inter-element distance d_t is employed (Figure 1b), the effective d_M becomes

$$d_{M,t} = d_t \min\left(|\cos\varphi|, |\cos(\pi/3 - \varphi)|\right),\ 0 \le \varphi \le 2\pi \tag{3.15}$$

leading to

$$d_{M,t} \le \sqrt{3}/2\ d_t = 0.866\, d_t \tag{3.16}$$

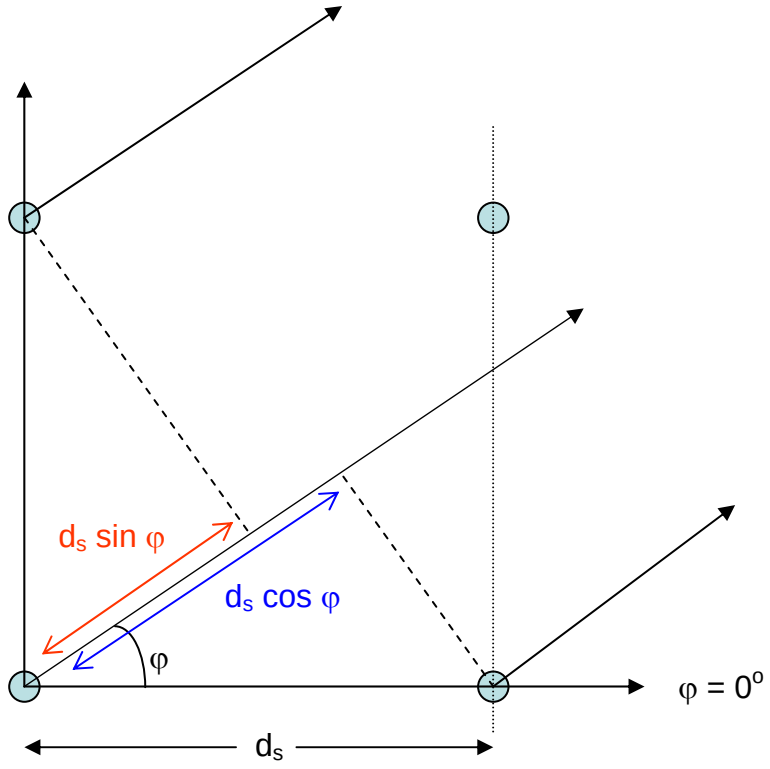

Figure 1a: Top view of four elements of a square grid planar array with inter-element distance d_s, showing how the effective inter-element distance d_M (which determines at which zenith angle grating lobes begin to appear) varies over the range (0.707 d_s … 1.0 d_s) as a function of the beam azimuth angle φ.

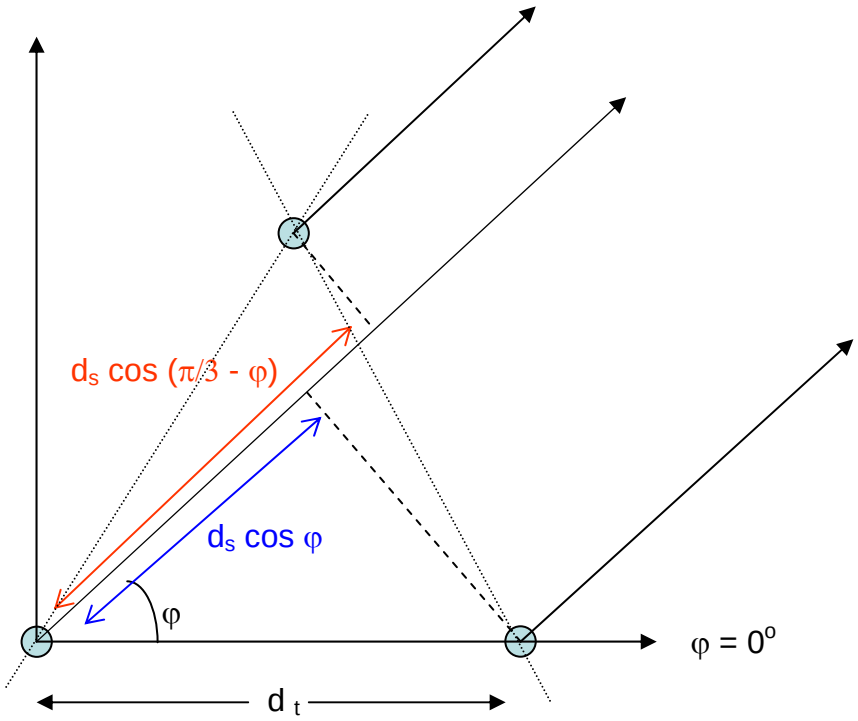

Figure 1b: Top view of three elements of an equilateral triangular grid planar array with inter-element distance d_t. In this geometry, d_M varies between 0.5 d_t and 0.866 d_t , reaching its minimum value for beam azimuth angles coinciding with the array grid line directions (i.e. for $\varphi = n \cdot \pi/3$, n = 0, 1, 2, 3….).

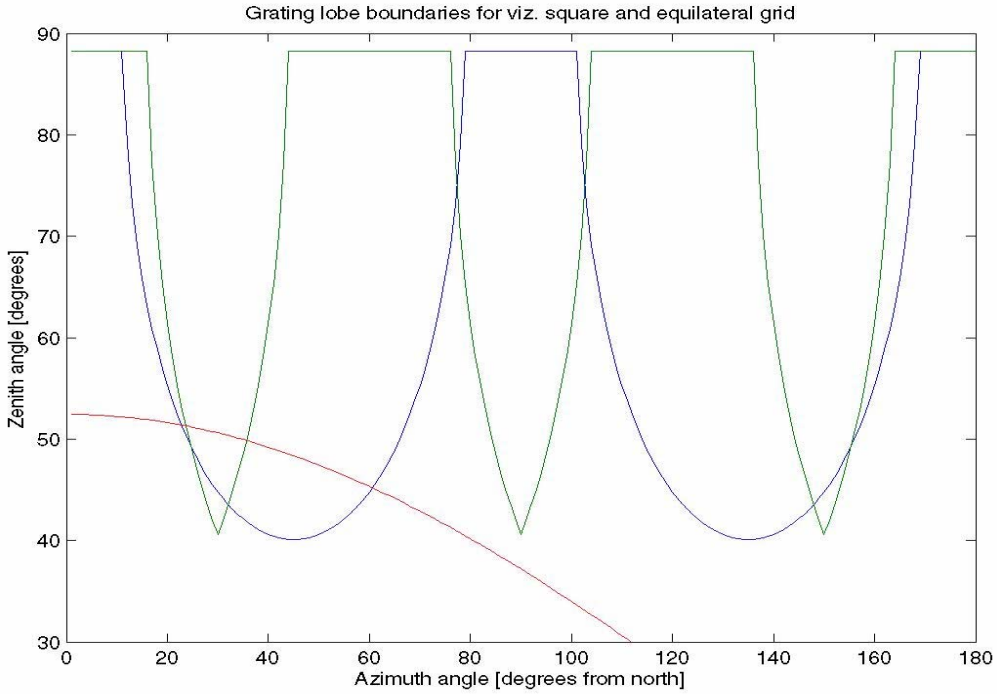

Figure 2: Showing the boundaries between grating-lobe-free and grating-lobe-contaminated regions of the visible hemisphere for two different arrays, viz. a square grid array with inter-element distance = 0.60 λ and the rows and columns oriented E-W and N-S respectively (blue), and an equilateral triangular grid array with inter-element distance = 0.69 λ and the rows oriented at ± 60^o to the N-S direction (green). The azimuth-zenith angle region below the respective curve is grating-lobe-free, while grating lobes are excited in the region above it. A safety allowance equal to 1.5 grating-lobe half-widths has been included to ensure that no part of an emerging grating lobe will appear in visible space. The red curve indicates the zenith angle of Cas-A, assuming that the arrays are located at 69^o N. This strong circumpolar celestial radio source will always be in the grating-lobe-free region of either array, except for two intervals of at most three hours each, equispaced on either side of northern culmination, and can be used as a reference for real-time adaptive pointing corrections.

In other words, for any given maximum zenith angle the equilateral grid geometry can use some 15 % greater inter-element distance than the square geometry and still remain grating-lobe-free at all azimuths.

Figure 2 shows the grating-lobe limits of two circular arrays, populated with isotropic radiators arranged in viz. a square configuration with d_s = 0.60 λ and an equilateral triangular configuration with d_t = 0.69 λ. These inter-element distances have been selected to make both arrays nominally grating-lobe-free out to 40^o. To make sure that not even the first sidelobe of a grating lobe complex will enter visible space, the plotted limits also include an extra safety margin equal to 1.5 grating-lobe half-widths.

The equilateral triangular configuration is seen to provide much larger grating-lobe-free solid angle coverage than the square one, while requiring about 13 % fewer elements per unit area than the square geometry. It is therefore recommended as the preferred 3D core array configuration.

3.3 Array pointing calibration and pointing corrections

All beam-forming and beam-steering in the EISCAT_3D system will be performed digitally by combining the several thousand data streams from the individual array elements with appropriate time delays to generate one or more beams in the desired direction(s). The first step in this procedure is the nulling out of system- and environmental-effects-dependent time offsets through the application of correction terms to all data streams individually.

Having established the set of first-order corrections required to form even an approximate beam, using GPS and other instrumentation, fine-tuning the corrections for optimum beam-shape and monitoring and adaptively adjusting the beam pointing will be realised through scanning a beam over the nominal positions of a number of strong celestial calibrator sources and constructing a pointing error matrix from the observed residuals. The EI_3D project is fortunate in this respect, as the two strongest (at 235 MHz) circumpolar sources, Cas-A and Cyg-A, are both in the grating-lobe-free region of the core array for a large fraction of the total time. With flux densities exceeding 6000 Jy at 235 MHz [9], a single properly focussed 49-element array sub-group (see below under Section 6) should see both sources at better than unity SNR. This suggests that an obvious way to calibrate the whole array is to first focus each sub-group separately and then adjust the relative time offsets between the cells for maximum SNR.

The red curve in Figure 2 shows the zenith angle of Cas-A at the planned location of the core site (approx. 69^{o} N). We note that if the equilateral triangular geometry is adopted, Cas-A will be in the grating-lobe-free region for nearly 22 hours out of every 24, the exceptions being two brief intervals either side of northern culmination, thus offering a possibility for almost continuous monitoring of the pointing performance.

With a declination of + 40^{o} 36', Cyg-A will spend about 50 % of the total time in grating-lobe-free parts of the visible hemisphere. It will be about 18 degrees lower in the sky than Cas-A at any given azimuth and therefore ideal for mapping out the beam at large zenith angles towards the south.

4. Element radiators

4.1 Electrical and practical considerations

Since the fully populated array will comprise several thousand elements, cost and logistics considerations argue strongly in favour of using the greatest possible inter-element separation consistent with meeting the overall system optical performance requirements, thereby keeping the number of element radiators as low as possible.

To get a rough idea of how far apart neighbouring radiating elements can be separated without running into trouble, we introduce the concept of *effective aperture* A_{em}. This is a fictitious area over which a radiator is assumed to extract all power from an incident RF field; a definition often found in the litterature is "the area which, when multiplied by the power density of the incident RF field, gives the power delivered by the antenna to a matched load" [10, p. 60]. An isotropic radiator has an effective aperture of $\lambda^2/4\pi$. Accordingly, for an antenna exhibiting a directivity D_0,

$$A_{em} = (\lambda^2/4\pi)D_0 \tag{4.1}$$

If the effective aperture can be assumed to be roughly circular, this corresponds to an effective aperture radius r_{em}:

$$r_{em} = \lambda/2\pi\sqrt{D_0} \tag{4.2}$$

Thus, to collect as much as possible of the power incident on an array aperture, the nearest-neighbour element distance should be $\cong 2\ r_{em}$. At this spacing, the effective apertures of neighbouring elements are just touching each other. Marginally larger spacings can often be used at the expense of a somewhat increased sidelobe level; much larger separations will result in the aperture being undersampled and power being lost.

Using (4.2) we compute the minimum element directivity corresponding to a given inter-element distance:

$$D_{0,\min} = (\pi\, d_o/\lambda)^2 \tag{4.3}$$

leading to

$$D_{0,\min} = 3.55 \ \ (5.5 \text{ dBi}) \text{ for } d_o = 0.6\lambda \tag{4.4}$$

and

$$D_{0,\min} = 4.83 \ \ (6.8 \text{ dBi}) \text{ for } d_o = 0.7\lambda \tag{4.5}$$

Two element radiator designs meeting the above minimum directivity requirements are viz. a dipole cross $\lambda/4$ above a ground-plane and a short (3 or 4 element) X Yagi-Uda antenna.

A thick half-wave dipole located $\lambda/4$ above a perfect, infinite ground-plane has a directivity of approximately 7 dBi [10, p. 147]; with two dipoles mounted at right angles to each other,

circular polarisation can be generated. Such X dipole / reflector combinations have been used as radiators in many phased arrays systems, one of the most recent examples being the SRI-developed AMISR/PFISR incoherent scatter radars now deployed at several locations in the western hemisphere.

Invented in the early 1920s, the Yagi is by now probably the world's most common gain antenna and used extensively throughout the HF, VHF and UHF frequency ranges. A gain-optimised three-element design, 0.4 λ long, can deliver up to 9 dBi gain over a narrow frequency range [10, p. 407]; more bandwidth can be had at the expense of moderate gain loss.

Practical and operational aspects must now be considered. Winter weather conditions at the envisaged 3D site, close to the present EISCAT Ramfjordmoen site in northern Norway, can change from sub-Arctic to maritime in a matter of hours. In midwinter, there can be long periods of extreme cold, causing a thick layer of hoarfrost to build up on exposed objects; later in the season, blizzards depositing up to a meter of wet, heavy snow in a day frequently hit the area. Experience from the EISCAT Heating system has shown that the snow layer can eventually become so heavy that its weight deforms the air-insulated aluminium coax feedlines running on low supports close to the ground.

To successfully handle these conditions, the whole 3D array should ideally be elevated at least some 2.5 m above ground level to provide room for a whole winter's accumulated precipitation underneath, so minimising the risk of the array becoming totally immersed in snow at the end of the season. This notwithstanding, the individual radiators must be designed so as to retain their electrical characteristics even when covered by a moderately thick layer of snow or ice (cf. the lessons from the ESR 42-m dish). The radiator system must also be so mechanically strong that it does not deform or collapse even under extraordinary weather conditions.

The horizontal X dipole-reflector combination does not fit these requirements very well at all. The reflector, which must cover essentially the whole array aperture, is a potential source of problems. While it can in principle be made lightweight by constructing it from wire netting, the netting mesh size can be selected no larger than approximately 0.055 λ or 70 mm if an acceptable approximation to a continuous ground-plane is required; a 70 mm mesh made from 3 mm wire will already exhibit a leakage of -14 dB, adding 10-12 K ground noise to the system temperature.

With a mesh size as small as 70 mm, snow and/or hoarfrost accumulating on the mesh wires will eventually fill the mesh completely; thereafter, the whole reflector area will start to collect snow. To prevent the reflector surface from becoming permanently deformed by the weight of the snow, sturdy, thick-wire netting must be used and access hatches, allowing the manual removal of snow from the upper reflector surface, must be installed at regular intervals. All this complicates the reflector and support structure design and offsets much of the weight and cost gain obtained by using netting in the first place. The anticipated need for regular snow-clearing is directly contrary to the 3D design goal of essentially unattended operation.

Short, thick-element Yagi antennas are likely to handle the Norwegian winter conditions better: A 20 mm diameter reflector element projects a surface area less than one-half that of a mesh-wire groundplane made from 3 mm wire and will therefore accumulate correspondingly

less snow. If however extraordinarily bad weather conditions should force a need for manual snow clearing, the absence of a continuous groundplane will allow this to be rapidly performed from the ground with simple tools (long brooms). From the practical point of view, therefore, a Yagi antenna with a minimum directivity of about 7 dBi is the preferred element radiator.

The logical next step was therefore to design, analyse, construct and validate a Yagi exhibiting the required qualities of moderate gain, large bandwidth, good circularity and relative insensitivity to weather effects. Unfortunately, the resources available to the existing Parties did not include any individual with extensive previous experience in numerical antenna simulations, nor access to electromagnetics software well suited to attack the analysis problem.

At this point the Project had a stroke of good luck. In early 2007, Mr. Toralf Renkwitz of Universität Rostock, Germany contacted EISCAT on his own initiative. Mr. Renkwitz, who was searching for a M. Sc. Eng. thesis project, already had hands-on experience of simulating Yagi antennas with the well-known NEC electromagnetics software suite. Plans for a detailed study of a number of 3-element X Yagi antenna designs were quickly formulated: NEC would be used to analyse their electrical and optical characteristics, numerical simulations of their performance as element radiators in very large arrays would be performed using a combination of NEC and Matlab, and a small test array would be constructed to verify the simulation results. The proposed study was submitted to the Institute of Information Technology, Universität Rostock for consideration and duly approved as the subject of Mr. Renkwitz's M. Sc. Eng. thesis; the EI_3D Technical Project Leader was appointed external thesis advisor.

After a brief introductory stay in Kiruna, Mr. Renkwitz proceeded with his work largely independently of other 3D activities. Recognising that his results could be of direct interest to the research conducted at the Institute of Atmospheric Physics (IAP) Kühlungsborn, the IAP kindly put its computing facilities, including its NEC software installation, at his disposal free of charge. After successfully completing his assignment, Mr. Renkwitz submitted and defended his thesis in June 2008. The thesis, an impressive 104-page document, is appended to this report and will be cited frequently in the following.

4.2 The "Renkwitz Yagi"

One of the primary tasks set for Mr. Renkwitz' thesis project was to derive accurate mechanical dimensions of at least one, if possible two, short (3-4 elements), X-Yagi antenna(s) suitable for use as element radiators and ideally having the following characteristics:

- Center frequency 235.0 MHz
- Bandwidth (specified as s_{11} < -20 dB) > +/- 6 MHz
- Relative gain of –1 dB at 40^o off-boresight, in all azimuth directions and over full bandwidth,
- Polarisation circularity better than –1 dB out to 30^o off-boresight, in all azimuth directions and over full bandwidth,
- Gain at angles > 75^o off-boresight as low as possible, but at least –16 dB,
- Element lengths < 0.4 λ while maintaining all other characteristics.

In Chapter 4 and Appendix A of the M. Sc. thesis [11], NEC-derived radiation patterns and electrical characteristics of three different 3-element Yagi configurations are presented and compared. A design using straight 20 mm diameter elements, a folded dipole radiator and a half-wave transmission line balun [10, p. 368] is identified as coming closest to the desired characteristics. This design, which in the following will be referred to as the "Renkwitz Yagi", is then used as the element radiator in the subsequent array simulations presented in Chapter 6. Its mechanical layout and dimensions and its simulated electrical characteristics are presented in Figure 3, Tables 1 and 2 and Figures 4 and 5 below.

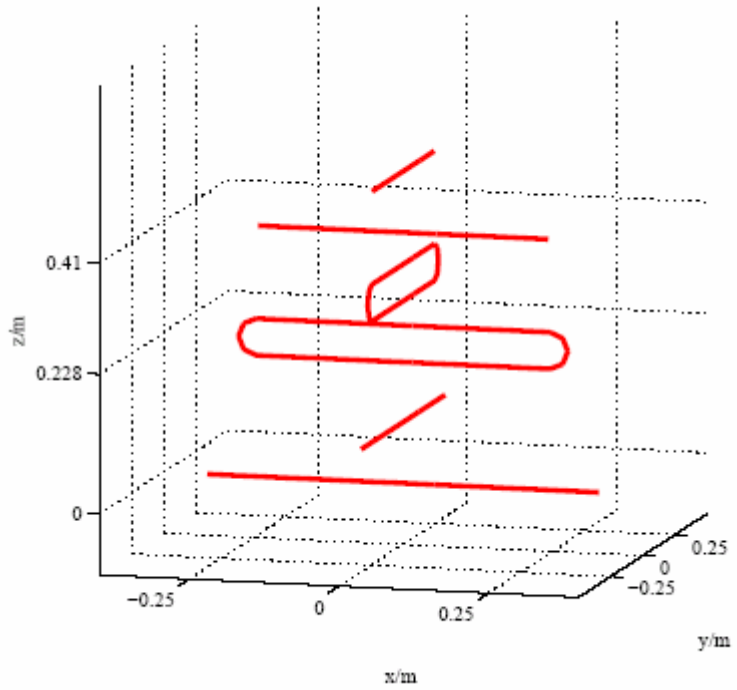

Figure 3: Scale drawing of the short 3-element X Yagi developed by Renkwitz (aka the "Renkwitz Yagi") and used as the element radiator in his array simulations. For constructional reasons, the two orthogonal sets of elements are offset lengthwise by ≈100 mm; the exact offset is uncritical and the resulting phase difference will be handled by the transmitter system.

Table 1: Renkwitz Yagi element lengths and positions

Element	Mechanical length	Position
Reflector	657 mm	0 mm
Folded dipole	550 mm	+ 228 mm (center)
Director	484 mm	+ 410 mm

Table 2: Predicted electrical and optical characteristics of the Renkwitz Yagi

Impedance	200 + j0 Ω
Gain	7.11 dBi
Main lobe FWHM	89°
Attenuation @ 40°	2.52 dB
Attenuation @ 75°	7.79 dB
Front/back ratio	20.1 dB
Bandwidth (s_{11} = -20 dB)	(-12.75 / +11.25) MHz
Bandwidth (Φ_Z= 5°)	(-9.00 / + 6.75) MHz

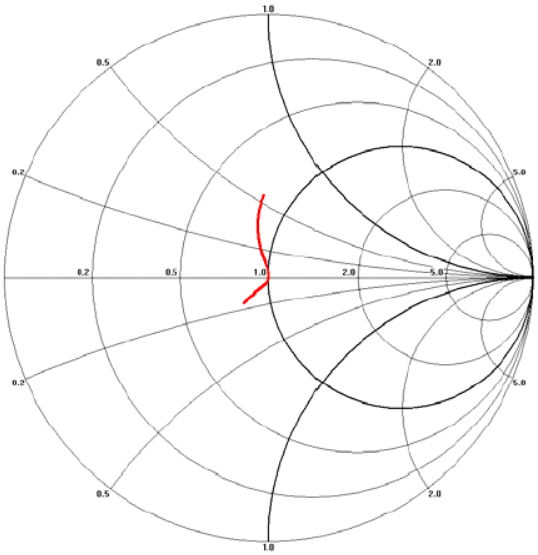

Figure 4: Predicted feedpoint impedance vs. frequency of the Renkwitz Yagi. The plot covers (220 – 250) MHz. Note the purely resistive impedance at mid-band.

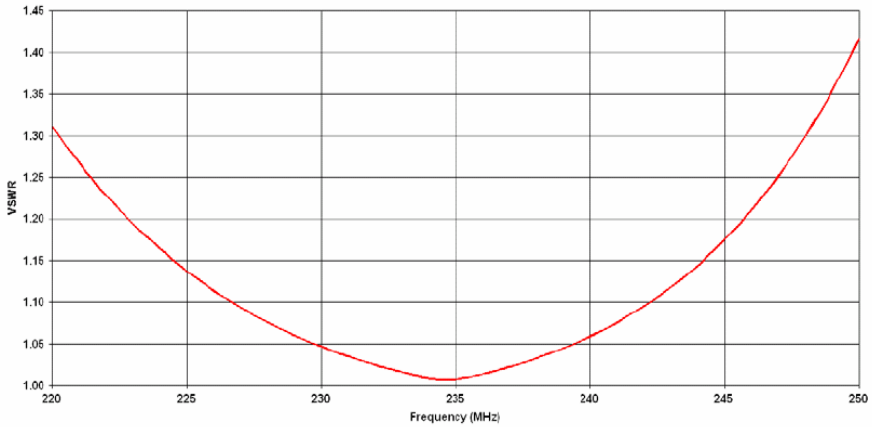

Figure 5: Predicted voltage standing-wave ratio (VSWR) vs. frequency of the Renkwitz Yagi. The passband is defined as the frequency range over which $s_{11} \leq$ -20 dB, corresponding to VSWR ≤ 1.22.

In general terms, snow and/or ice collecting on the elements of a Yagi or any other parasitic-element antenna will lower the resistive component of the feedpoint impedance and cause a downward shift of the resonant frequency, paired with a narrowing of the passband. The antenna pattern will also be affected to some degree. The effects of ice on the feedpoint impedance and passband of the Renkwitz Yagi have been investigated in a separate series of simulations [11, pp. 44-46]. The expected passband shape when the antenna is covered by a smooth 3 mm thick ice layer with $\varepsilon_r = 5$ and conductance $G = 4 \cdot 10^{-4}$ S/m is shown in Figure 6. The expected downward shift of the passband is clearly visible; the s_{11} = -20 dB / VSWR = 1.22 points are shifted from 222.5 MHz to 220 MHz and from 246.5 MHz to 241.5 MHz, respectively.

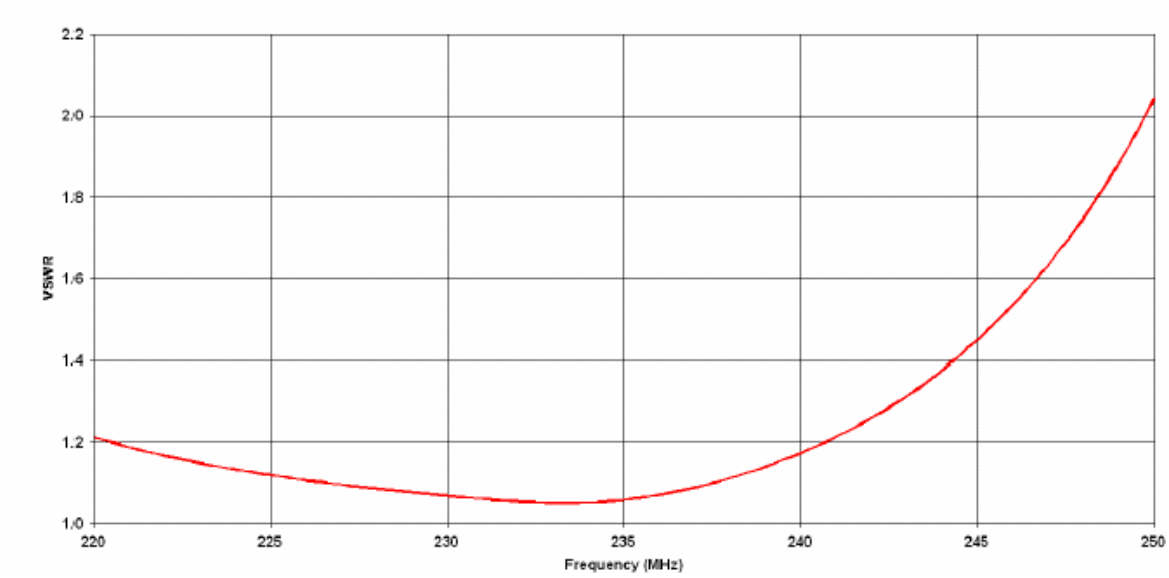

Figure 6: Predicted voltage standing-wave ratio (VSWR) vs. frequency of the Renkwitz Yagi when covered by a 3 mm thick layer of ice with $\varepsilon_r = 5$. The $s_{11} \leq$ -20 dB / VSWR $\leq$ 1.22 passband is shifted downwards by close to 4 MHz relative to that of an ice-free antenna, but still meets the design target of $s_{11} \leq$ -20 dB over (235 ± 6) MHz.

4.3 Experimental validation of simulations; measurement data

To validate the simulation results, a full-size Renkwitz Yagi employing tuneable dipoles has been constructed to the dimensions given in Table 1 (see Figure 7). The elements are passed through the 30-mm square boom and welded to it on both sides to create a sturdy structure and ensure positive electrical contact. In this configuration, the boom exerts a small shortening effect on the elements, which are therefore lengthened by a few mm according to Renkwitz' Table 4.7 [11, p. 43].

Complex impedance measurements have been carried out on the test antenna, using a vector network analyser. The results obtained after fine-tuning the dipole shorting bar positions, shown in Figures 8 and 9, are in very good agreement with the simulated performance in Figures 4 and 5. A 19-antenna test bed for validation of the mutual coupling behaviour predicted in [11, pp. 49-62] is presently under construction. Measurement data will be published separately before the end of the 3D project.

Figure 7: The first 235-MHz X Yagi, constructed to the mechanical specifications given in Table 1, under typical midwinter conditions. In this beta version, the folded dipoles are made with movable shorting bars to allow a limited amount of fine-tuning. The production run antennas will have their dipoles made from formed continuous lengths of aluminium tubing. The blue cables that are strapped down onto the boom are half-wave baluns transforming the nominal 200 ohm balanced feedpoint impedance to 50 ohms unbalanced.

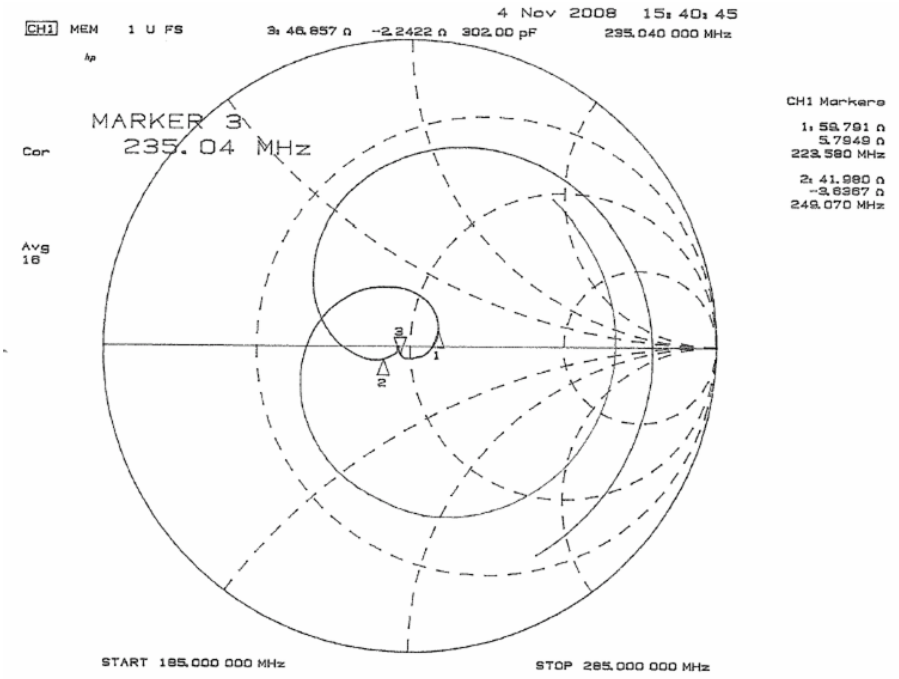

Figure 8: Smith diagram plot of the measured terminal impedance Z of the front half of the Renkwitz Yagi evaluation model. The predicted reactance sign reversal at mid-band (the "cusp") is clearly visible next to marker # 3. The reference plane for this measurement is at the end of a piece of 50-ohm coax, extending backwards from the feedpoint to a point approx. 30 cm behind the reflector element, so the impedance vs. frequency trace appears rotated relative to the predicted one.

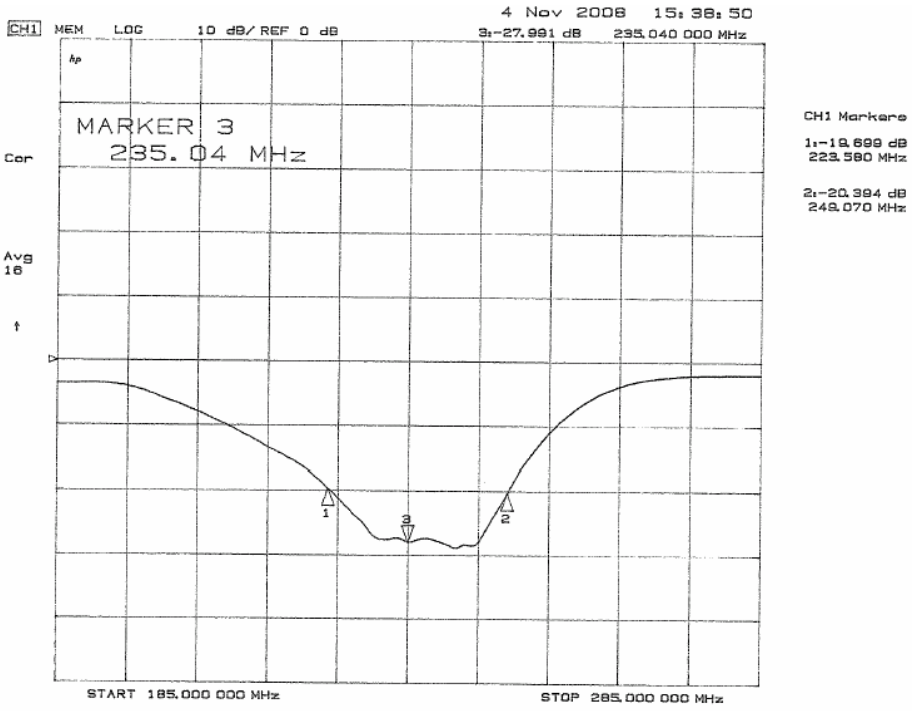

Figure 9: Reflection coefficient $\mathbf{s}_{11}$ magnitude vs. frequency for the front half of the evaluation model Renkwitz Yagi. The measured -20 dB $\mathbf{s}_{11}$ bandwidth, (- 11.4 / + 14.0) MHz slightly exceeds the predicted one but is shifted upwards in frequency by about 2.5 MHz relative to mid-band. The reason for this is being investigated.

Figure 10a: Reflection coefficient $\mathbf{s}_{11}$ vs. frequency for an ice-free Renkwitz Yagi. The -20 dB $\mathbf{s}_{11}$ pass-band is approximately (222-248) MHz.

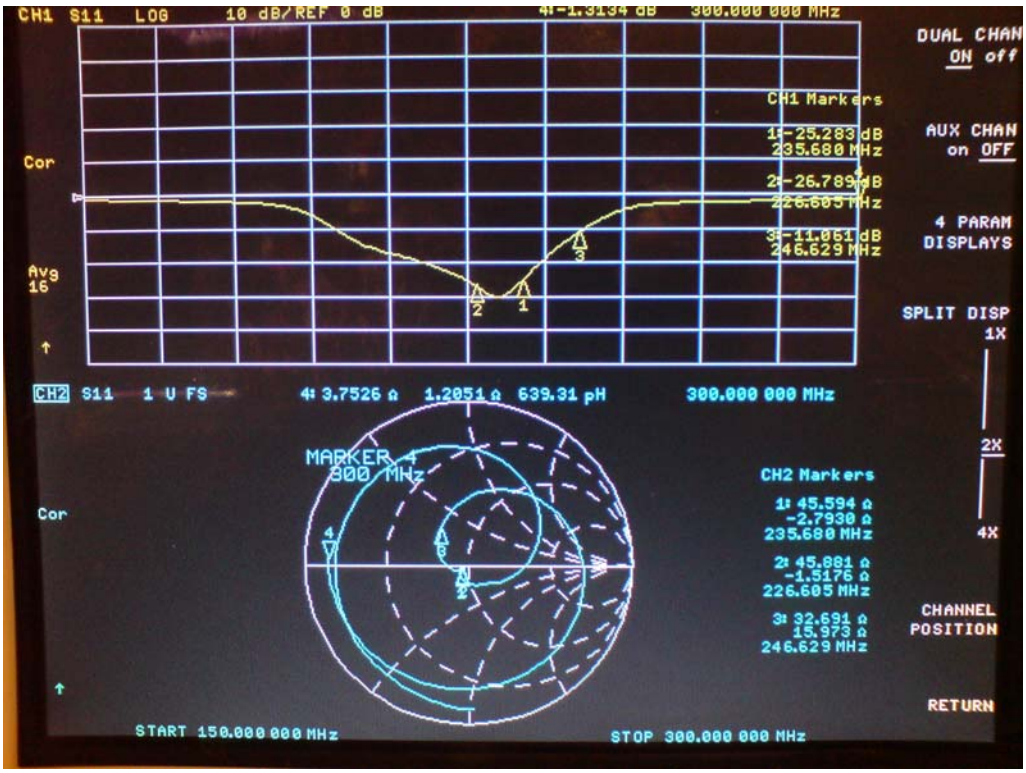

Figure 10b: Reflection coefficient $\mathbf{s}_{11}$ vs. frequency for the same antenna covered by an approx. 2.5 mm thick ice layer, applied by repeatedly spraying water onto the antenna elements with a spray bottle. For this measurement the antenna was kept at an ambient temperature of - 15^{o} C. The -20 dB $\mathbf{s}_{11}$ pass-band has now shifted to approx. (216 – 239) MHz and no longer meets the (235 ± 6) MHz band-width requirement on the high-frequency side.

In a separate measurement series, the antenna behaviour under ice load has been investigated experimentally. A single-polarisation test antenna, sitting on its outdoor test stand at an ambient temperature of -15^{o} C, was repeatedly sprayed with tap water to allow an ice layer to form on all elements, and the feedpoint impedance was measured for every 0.5 mm of additional ice thickness. Figures 10a and b illustrate the observed effect.

In Figure 10a, the antenna elements are still clean and the passband is essentially identical to that of the ice-free X yagi (Figures 8 and 9). In 10b, the whole antenna is covered by a 2.5 mm thick ice layer. While not quite identical with the simulated results of Figure 8, the measured $|\mathbf{s}_{11}|$ pass-band shapes are very similar, indicating that the simulation gives a fair representation of the situation likely to be found in practice.The -20 dB $\mathbf{s}_{11}$ points have now shifted downwards in frequency to approx. 216 and 239 MHz. Thus, while the ice-loaded antenna still exhibits a bandwidth far exceeding 12 MHz, it no longer meets the -20 dB $\mathbf{s}_{11}$ requirement at 241 MHz, the nominal upper band edge.

This can however be easily remedied. Since the actual -20 dB $\mathbf{s}_{11}$ bandwidth is almost 25 MHz, a series-production design could be optimised for a center frequency about 2.5 MHz above the nominal band center, i.e. 237.5 MHz. This modification should ensure that the upper passband edge stays well above 241 MHz even when the antenna is covered by a 2.5 mm ice layer; the associated gain loss at 235 MHz should be almost unnoticeable under normal (ice-free) conditions.

5. Radar time resolution in incoherent-scatter mode vs. array size

Below, we compare the *power-aperture products* of a range of different size 3D core arrays to that of the EISCAT VHF radar system, which will be used as a performance reference in the following.

The power-aperture product Π, i.e. the product of peak transmitter power and receiving antenna aperture, is often used to rate the relative performance of radar systems. In a mono-static phased array system, where the array is shared by the transmitter and the receiver, transmitter power and receiving antenna aperture area both increase linearly with the number of elements, assuming all elements are driven and no aperture tapering is applied. In this case, the power-aperture product goes as the square of the number of elements.

The VHF system [12] is EISCAT's most powerful radar. It can be configured either as a single-beam system (Mode 1) or, by rearranging the feed system, as a dual-beam system where one-half of the antenna aperture and one-half of the transmitter power are dedicated to each beam (Mode 2). In Mode 1, $\Pi \cong 9.8$ GW m^2; in Mode 2, $\Pi \cong 2.5$ GW m^2 for each of the two beams. In both modes, the power density at the antenna aperture is 0.94 kW m^{-2}.

Following 3.2, the 3D core array is assumed to be a circular, filled array of Renkwitz Yagis arranged on an equilateral triangular grid with an inter-element distance $d_{o,t} = 0.70\ \lambda \cong 889$ mm ($f = 236$ MHz). Since the radiation pattern of the Renkwitz X Yagi is down by -5 dB or more over the entire $(60 - 90)^o$ zenith angle range and displaying a deep null at $(85\text{-}90)^o$, the inter-element distance can be increased from $0.69\ \lambda$ to $0.70\ \lambda$ without running into difficulties; as the main beam zenith angle approaches 40^o, the element pattern will suppress any grating lobes by several dB as they first appear on the horizon.

Using (3.3) and (3.10) we find that $n_{\alpha d}$, the number of array elements required to produce a beam with a given opening angle α_d (expressed in degrees), is

$$n_{\alpha d} \approx 9080\,\alpha_d^{-2} \tag{5.1}$$

The associated array diameter is

$$D_{\alpha d} = 8.88\,\alpha_d^{-1} \tag{5.2}$$

Assuming a peak transmitter power per element = 600 W, the power-aperture product becomes

$$\Pi_{\alpha d} = 6.0 \cdot 10^{-4}\, n_{\alpha d} \quad [\text{MW m}^2] \tag{5.3}$$

$n_{\alpha d}$, $D_{\alpha d}$ and Π of some arrays are tabulated in Table 3 below.

Note that an array of ≈ 5000 elements will deliver a power-aperture product about equal to that of the VHF operating in Mode 1, paired with a beam-width smaller than that of the VHF operating in Mode 2. In other words, an aperture array less than one-third the size of the full projected 3D core will match the performance of the current VHF system and could replace most of its functionality if required.

Table 3: Parameters of some λ = 1.27 m (f = 236 MHz) phased arrays. Equilateral grid geometry, Inter-element distance = 0.7 λ, transmitter power 600 W / element

Array #	Beam FWHM [deg]	Number of elements	Array diameter [m]	Power-aperture product [GW m^2]	Notes
1	3.0	1009	29.6	0.4	1
2	2.0	2270	44.4	2.1	4
3	1.2 x 1.7			2.4	2
4	1.5	4036	59.2	6.7	
5	0.6 x 1.7			9.8	3
6	1.25	5811	71.0	13.8	
7	1.0	9080	88.8	33.7	
8	0.75	16142	118.4	106.6	
9	0.5	36320	177.6	539.8	4

Note 1: Minimum size phased array, comparable to the ESR Phase 1 system
Note 2: EISCAT VHF, Mode 2 (dual beam, power-aperture product per beam)
Note 3: EISCAT VHF, Mode 1 (full antenna, single beam, 2.4 MW)
Note 4: Cf. the EISCAT UHF (32 m parabolic dish, $\theta = 0.6^o$, 2 MW @ 928 MHz), whose power-aperture product is only 1.1 MW m^2

We next investigate which, if any, of the tabulated arrays will meet the 3D target incoherent scatter time resolution performance as specified in 2.12. Starting from the diffuse, beam-filling-target monostatic radar equation [13, p. 59], an approximate expression for the incoherently scattered power received from a slab of plasma of thickness h, located at a distance R and filled with plasma of average density n_R, is:

$$P_r = \Pi\, n_R\, h\, \sigma_o \sin^2 \chi / 4\pi R^2 \tag{5.4}$$

where Π is the radar power-aperture product, σ_o is the electron radar cross-section, χ is the polarisation angle and R is the range from the radar to the target volume.

In the receiver system, this information-carrying power competes with noise power from a number of sources. At the planned 3D operating frequency (235-240 MHz), about 75-80 % of the total noise power is of galactic origin and picked up by the antenna; the remainder is generated internal to the receiver. Over the bandwidth in question (a few tens of kHz) the noise spectrum can normally be regarded as flat, so the noise power can be estimated using the thermal noise approximation:

$$P_N = \kappa T_N B \tag{5.5}$$

where κ is Boltzmann's constant, T_N the equivalent blackbody noise temperature and B the bandwidth. At 240 MHz and 68^o N latitude, a realistic mean T_N is ≈ 190 K.

The radar pulse length τ defines the plasma slab thickness h:

$$h = ½ c \tau \tag{5.6}$$

In order to recover most of the energy contained in a pulse of duration τ, the receiver bandwidth B must be matched to the pulse power spectrum:

$$B \cong 2/\tau = c/h \tag{5.7}$$

The noise power picked up by the receiver over this bandwidth is

$$P_N = c\kappa T_N / h \tag{5.8}$$

The instantaneous (single-pulse) signal-to-noise ratio is therefore

$$SNR_1 = \frac{P_r}{P_N} = \frac{\Pi n_R h^2 \sigma_o \sin^2 \chi}{c\kappa T_N 4\pi R^2} \tag{5.9}$$

Factoring out all constants, this can be rewritten as

$$SNR_1 = \frac{\sigma_o \sin^2 \chi}{4\pi c\kappa} \cdot \frac{\Pi n_R h^2}{T_N R^2} \tag{5.10}$$

For a monostatic radar $\sin^2 \chi$ =1, so

$$SNR_1 = 1.92 \cdot 10^{-15} \cdot \frac{\Pi n_R h^2}{T_N R^2} \tag{5.11}$$

Inserting T_N = 190 K this can be further simplified to

$$SNR_1 \approx 10^{-17} \frac{\Pi n_R h^2}{R^2} \tag{5.12}$$

At low SNR, the variance of a noise-corrupted (*S*+*N*) measurement is dominated by the noise variance. This can be reduced by time-averaging a number of statistically independent measurements. For Gaussian white noise the resulting variance is equal to the noise mean divided by the square root of the number of averaged independent measurements, *N*:

$$\mathrm{var}_N = \frac{1}{SNR_1 \sqrt{N}} \tag{5.13}$$

One might naively assume that as the signal-to-noise ratio increases, the variance should eventually approach zero, but this is not the case. Because the plasma processes manifested in the incoherent scatter spectrum are stochastic, a large number of independent spectral measurements must be averaged in order to obtain meaningful estimates of the different spectral moments. Again, the variances of these averaged estimates drop off as $N^{-0.5}$.

The intrinsic correlation time of the plasma, t_c, now sets an upper limit on the rate of statistics that can be obtained: for consecutive measurements to be statistically independent, they must be separated in time by at least the correlation time. At 150 km height and 235 MHz radar frequency, t_c is in the order of a millisecond. Accordingly, the 1 kHz pulse-repetition

frequency specified in the PSD Section 2.12 for measurements at that height is in fact the maximum that makes sense and should reasonably be employed.

Section 2.12 of the EISCAT_3D Design Specification Document specifies target time resolution values at different altitudes and 10 % electron density uncertainty. For the low SNR values in question, the uncertainty can be assumed to be almost entirely due to noise variance; so

$$N > (10/SNR_1)^2 \tag{5.14}$$

Using numerical values from Section 2.12, we now compute approximate values of single-pulse SNR and *N* for System 8 and System 9 in Table 3. The pulse roundtrip times to 150, 300 and 800 km range are respectively 1, 2 and 5.3 milliseconds, so at most 187 independent measurements per second can be obtained from 800-km, 500 from 300-km and 1000 from 150-km. The results are tabulated below:

Table 4: Single-pulse SNR, integration times and *N* (10% uncertainty) for System # 8 (SNR corrected for T_e/T_i)

R [km]	n_R [m^{-3}]	T_e/T_i	h [m]	$n_R h^2/R^2$	$t_{int,\ target}$ [s]	$SNR_{1,8}$	N_8	$t_{int,\ actual}$ [s]
150	1×10^{10}	1.0	100	4.4×10^3	1	2.2×10^{-3}	2.1×10^7	9200
300	3×10^{10}	2.0	300	3.0×10^4	1	1.7×10^{-2}	3.5×10^5	700
800	3×10^{10}	3.0	1000	4.7×10^4	10	1.3×10^{-2}	6.4×10^5	3400

Table 5: Single-pulse SNR, integration times and *N* (10% uncertainty) for System # 9 (SNR corrected for Te/Ti)

R [km]	n_R [m^{-3}]	T_e/T_i	h [m]	$n_R h^2/R^2$	$t_{int,\ target}$ [s]	$SNR_{1,9}$	N_9	$t_{int,\ actual}$ [s]
150	1×10^{10}	1.0	100	4.4×10^3	1	1.1×10^{-2}	8.3×10^5	830
300	3×10^{10}	2.0	300	3.0×10^4	1	8.4×10^{-2}	1.4×10^4	28
800	3×10^{10}	3.0	1000	4.7×10^4	10	6.3×10^{-2}	2.5×10^4	133

We see to our dismay that a System 8 configuration using short single pulses under Section 2.12 conditions falls hopelessly short of the target. Even a System 9 configuration fails to meet the desired time resolution at all altitudes; at 150-km by a factor of over 800! This highlights the need for running the system with advanced modulation schemes at all times, as this will allow the extraction of a substantial number of essentially uncorrelated target estimates from each radar cycle, corresponding to a reduction in the required integration time by factor of ≈ 10.

However, this still leaves a huge discrepancy between the desired time resolution and that actually achieved. To make up for this on the system side would take a core array having a power-aperture product ≈1500 GW m^2, that is, about three times that of the System 9 array. Apart from the dramatically increased construction cost that this would entail, it is probably unrealistic to aim for this level of performance also for technical reasons. Raising Π by adding more elements to the array will push its near-field limit out to about 80 km, thus putting the whole D region into the near field, which will require altitude-dependent refocussing to be

applied to all signals received from this range; attempting to raise Π by tripling the output power of each power-amplifier module will raise their power dissipation to a point where waste heat management becomes a serious problem.

Instead, let us now turn the problem on its head and consider how much the height resolution would have to be relaxed, i.e. the slab height *h* increased, to make a System 8 configuration meet the 1/10-second time resolution requirement.

According to Equation (5.13), $N \propto SNR_1^{-2}$ and from Equation (5.11) $SNR_1 \propto h^2$ =>

$$N \propto 1/h^4 \tag{5.15}$$

Increasing the slab height by a factor of (2…10) thus puts a System 8 configuration squarely back in business as far as time resolution is concerned, as Table 6 below shows:

Table 6: Single-pulse SNR and integration times for 10% uncertainty for a System # 8 configuration. Height resolution at each altitude adjusted to bring the integration time below the target value. Scattering cross sections corrected for T_e/T_i effects.

R [km]	N_T [m^{-3}]	T_e/T_i	h [m]	$N_T h^2/R^2$	$t_{int,\ target}$ [s]	$SNR_{1,8}$	N_8	$t_{int,\ actual}$ [s]
150	1×10^{10}	1.0	1000	4.4×10^5	1	2.2×10^{-1}	9.2×10^2	0.92
300	3×10^{10}	2.0	2000	1.3×10^6	1	4.7×10^{-1}	4.5×10^2	0.89
800	3×10^{10}	3.0	5000	1.2×10^6	10	3.1×10^{-1}	1.0×10^3	5.5

The SNR is now well over 20 % at all altitudes, which already brings us into the region of diminishing returns; however, any substantial improvement in altitude resolution will require significantly longer integration times.

Table 6 thus gives a fair representation of the practical performance limit of a System # 8 (16000-element) array. The user community is strongly advised to consider it and review its requirements accordingly. In particular, keeping in mind that demands for extreme simultaneous time and height resolution must be paid for at very high capital investment and operating cost, agreement on whether incoherent-scatter altitude resolutions better than 1 km are really meaningful and required at altitudes above 150 km must be reached before the 3D project proceeds to the RFQ phase.

6. Practical construction aspects and trade-offs

As shown in section 5 and Tables 3 and 6, more than 16,000 array elements will be required to approach the full 3D array target performance specification. In addition to the actual antenna (a Renkwitz Yagi), each element comprises a dual 300-watt RF power amplifier, a direct-digitising receiver and a data processing unit. These sub-systems, which are scattered throughout the array, must all be installed in weatherproof housings and provided with electrical power, full-duplex high-speed data communication channels and reference time and frequency signals. Distribution grids for these services must be put in place before, or concurrently with, the construction of the actual array.

With such a large number of elements, an array architecture where each element is a self-contained unit is clearly impractical and some degree of sub-grouping must be considered. If the array is subdivided into sub-groups or cells of (10…100) element radiators, with all electronics subsystems housed in a single equipment container per group, the overall system complexity is reduced dramatically and substantial cost savings can be expected to result. Assuming N_R radiators per group, the number of equipment containers, power distribution boards, data network nodes and time and frequency distribution cables would all be reduced by the same factor N_R.

The equilateral grid structure proposed for the 3D array lends itself naturally to a self-similar grouping scheme. Any array element and its six nearest neighbours can be circumscribed by a regular hexagon. In turn, seven of these hexagons can be circumscribed by a larger hexagon with seven times the area and 49 elements, and so on in hierarchical order. In the following, it is therefore natural to consider a progression of sub-group sizes in the order 7, 49, 343, 2401, 16807 elements per sub-group, where the last group is essentially equal to the full array. Figure 11 illustrates how seven 49-element sub-groups can be combined into a close-packed 343-element group.

A consequence of concentrating all electronics to a single equipment shelter per sub-group is that the radiator elements (Yagis) must be connected to their respective RF units through some meters of coax cable. In the receive mode, the cable loss will act as a thermal noise generator that raises the system noise temperature somewhat. As an example, at 240 MHz foam-filled LCF 78-50 Cellflex cable (the standard cable used for 3G mobile phone base station installations) exhibits a loss of 0.028 dB/m; at 290 K ambient temperature, this corresponds to a noise temperature of 1.9 K/m.

Equation 5.13 shows that at low signal-to-noise ratios, the integration time required to reach some specified variance is proportional to SNR^{-2}. A small system noise temperature increase of, say, x % will therefore result in ≈ 2 x % increase in the integration time. We are now faced with a linear-programming problem: what is an acceptable compromise between subgroup size and cable-loss-induced loss of statistics?

The system noise temperature, T_{sys}, is the sum of several contributions:

$$T_{sys} = T_{sky} + T_{spillover} + T_{cable} + T_{TR} + T_{rec} \tag{6.1}$$

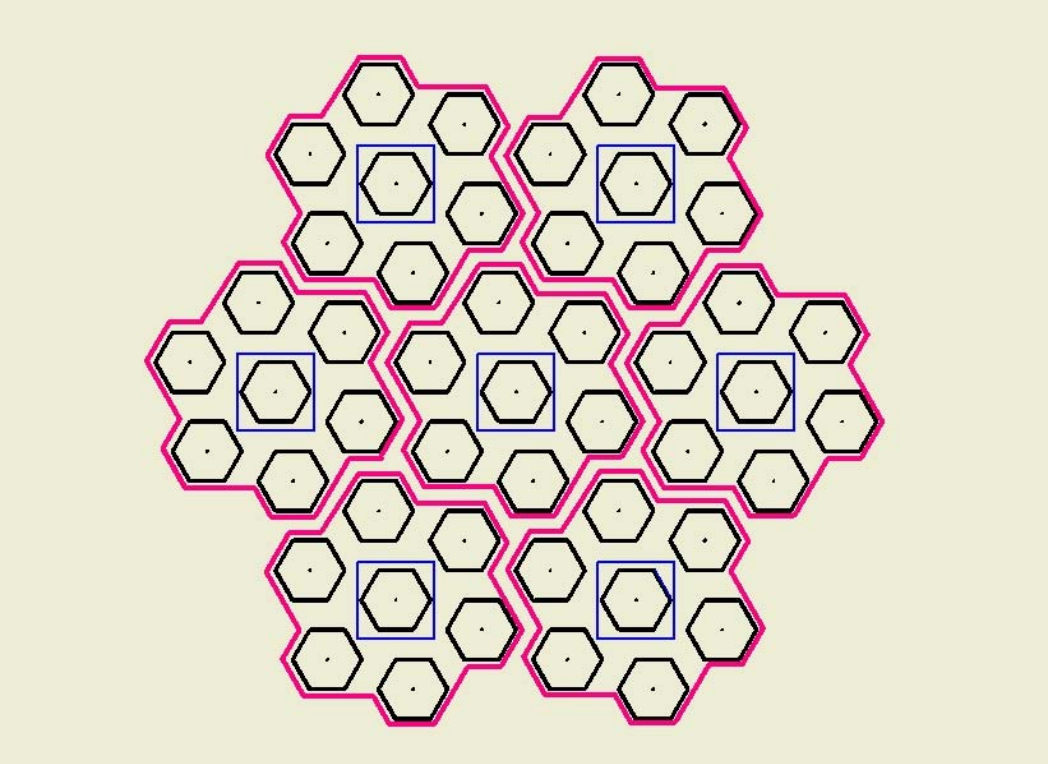

Figure 11: Illustrating how the 3D core array can be built up from close-packed 49-element sub-groups, each of which can be regarded as composed of seven 7-element hexagonal cells. The Figure shows a top view of a 343-element, approximately 18-m diameter array group, formed from seven sub-groups (outlined in red). Each sub-group is served by a common, approx. 2-m by 2-m equipment container (indicated by a blue square at the centre of each sub-group) containing all RF, signal processing and control and monitoring electronics.

In the VHF range, T_{sky} is by far the largest contributor and sets the ultimate sensitivity of the receiving system. At 235 MHz and 69^o N latitude (i.e. the latitude of the 3D core site), it never drops below 100 K; for more than 50% of the time it exceeds150 K. $T_{spillover}$ represents the noise picked up by the antenna through all its other lobes. In the present case, $T_{spillover}$ is estimated at about 20 K, most of which is thermal ground noise picked up through the array back-lobe.

The target noise temperatures of the T/R switch and the receiver are 15 K and 35 K, respectively, leading to

$$T_{sys} \geq [100 + 20 + 15 + 35]K + T_{cable} = 170K + T_{cable} \qquad (6.2)$$

The cable lengths required for different size sub-groups are estimated by first averaging the radial distances from all antennas in a cell to the common equipment shelter (refer to Figure 10) and then adding 1.6 m to account for the vertical separation between antenna and shelter. The cable lengths and the resulting noise temperature contributions and integration time increases are listed in Table 7 below. If we – somewhat arbitrarily – decide that cable noise shall not be allowed to reduce the rate of statistics by more than 10% compared to a

hypothetical lossless feed system, even under worst-case conditions, the 49-element cell becomes the obvious choice.

Table 7: Average (equipment shelter – antenna) cable lengths and corresponding cable noise contributions and integration time increases for constant variance as function of cell size, assuming hexagonal cells with inter-element distance 0.889 m and LCF 78-50 cable.

# elements / cell	# cells needed for full 16K array	Average cable length [m]	Average T_{cable} contribution [K]	Integration time increase [%]
7	≈ 2300	1.6	3.0	3.6
49	≈ 330	3.0	5.7	6.8
343	≈ 48	10.5	20.0	25.0

Figure 12 gives an artist's impression of how a 343-element array group, configured as seven 49-element cells, could be organised. The containers in this figure are approx. 2.0 x 2.0 x 2.8 m, so allowing engineers and technicians to stand erect inside them when checking or servicing equipment.

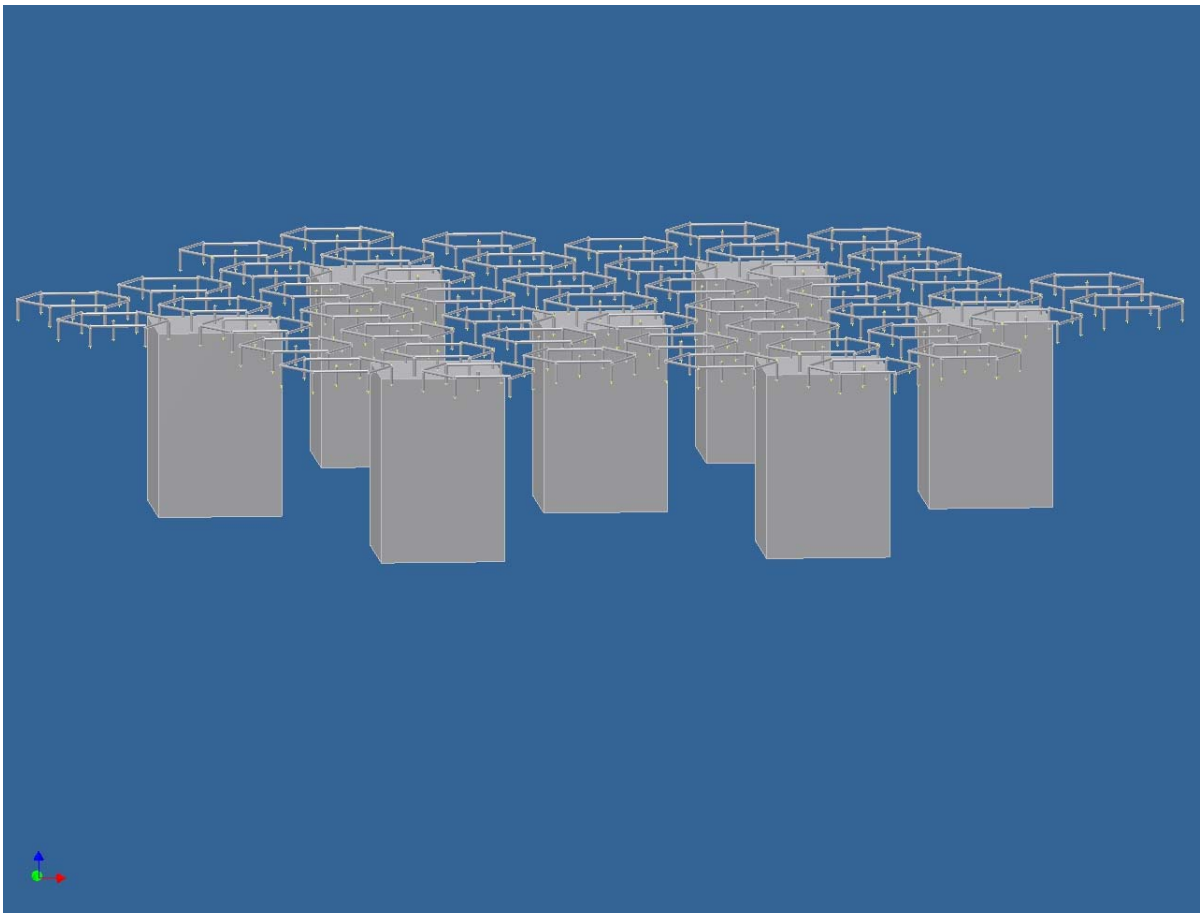

Figure 12: A side view of the 343-element array group of Figure 11. Each hexagon denotes a seven-element cell, comprising six element radiators at its corners and one at its center. The array is assumed to be elevated at least 3 m above average ground; the actual element radiators and the array support structure are suppressed for clarity. Seven 2 x 2 x 2.8 m equipment containers, each serving 49 radiators, are situated under the array.

A centre-to-centre distance between neighbouring cells of about 6.2 m will allow a technician to drive in between the containers with a 4x4 motorcycle and a trailer to bring in measurement equipment and/or remove failed units when required. Power and data distribution complexity is reduced 49-fold compared to a fully ungrouped system. Assuming 60 % DC-to-RF conversion efficiency and 20 % transmitter duty cycle, the 49 transmitters in each container will consume an average of 10 kW. Further assuming that the house-keeping power can be kept below 5-6 kW and that cosφ can be maintained below 0.9, a standard 3-phase 400 V, 25 A power feed per container will be sufficient.

With a inter-cell distance of 6.2 m or 4.9 λ, the 49-element cell is also a very suitable size for the interferometry application, providing a fair approximation to the shortest (6-λ) baseline and a very good match to the 15-λ and 30-λ baselines. Since the array does not need to be resolved down to a fraction of the cell size, the data from all 49 elements can be merged before sent off to the central processor. By installing a 49-input FPGA-based beamformer in each equipment container, the outgoing data rate can be reduced by a factor of $49/n_b$, where n_b, the number of simultaneous beams, is likely to be ≤ 5 (one active beam, aligned with the transmitted beam, three "monopulse" beams skirting the main beam at three equispaced points, and one pointing-calibration beam). In normal circumstances, the total outgoing data rate from each container will therefore be some 12 – 13 Gbit/s maximum.

7. The receiver subsystem

There are essentially two alternative ways to implement the active element receiver function: it can either be included as a distinct subsystem, or it can be integrated with the TX exciter and HPA into a combined RF unit, transceiver style.

As far as receiver performance is concerned, the requirements are largely the same in the active element as in the receive-only arrays, but with one very important exception: Since the transmit-receive switching system can never be made completely "watertight", leakage power from the transmitter in the order of (-10…0) dBm will be impressed on the active element receiver during each transmission. The receiver must therefore be capable of sustaining this pulsed leakage indefinitely without degradation. It must also recover very fast (<<10 μs) from the resulting severe overload. Meeting these requirements is mainly a matter of careful active device selection and bias circuitry design and should be neither difficult nor costly if designed-in from the beginning.

Other mono-static phased-array research radar systems, e.g. the Japanese 50 MHz MU radar [14] and the 440 MHz AMISR/PFISR [15], have chosen the transceiver approach for obvious reasons (they have no receive-only arrays).

For the 3D system the choice is not clear-cut. One could imagine a hybrid system comprising both transceiver modules at the core site and straight receivers at the outlier sites, or a system where all receivers are identical. To decide between these alternatives, it is instructive to consider how many receivers will be required altogether, and how many of those will belong to the active element.

Assuming an orthogonal array grid and a core element separation of 0.7 λ, the number of elements required to fill an aperture area A_C is N_C:

$$N_C = A_C / (0.7\lambda)^2 \tag{7.1}$$

The receive-only arrays will be required to observe only over a relatively restricted part of the visible hemisphere, typically within a cone having an apex angle of about 40^o. The element antennas can therefore be e.g. short Yagis with a gain in the order of 10 dBi, separated by about 1.25 λ in the plane orthogonal to the array boresight direction and by about (1.25 λ / sin ε) along the projection of the boresight direction in the horizontal plane, where ε is the element antenna elevation.

It follows that N_R, the number of element antennas in a remote array, is

$$N_R = A_R \sin\varepsilon / (1.25\lambda)^2 \tag{7.2}$$

where A_R is the receive-only array ground area.

For the sake of argument, let us assume that all arrays have the same physical aperture size, i.e. that $A_R = A_C$. A system comprising a core array and four receive-only arrays elevated to $\varepsilon = 55^o$ will then contain a total of N_{RX} receivers:

$$N_{RX} = A_C \frac{\left[(0.7)^{-2} + 4 \cdot (1.25 \sin 55^\circ)^{-2}\right]}{\lambda^2} = A_C \frac{2.041 + 3.815}{\lambda^{-2}} = 5.86\, A_C / \lambda^2 \qquad (7.3)$$

where the two terms in brackets are proportional to the number of receivers in the core and the number of receivers in the receive-only arrays respectively.

Thus, in a full five-site 3D system with orthogonal geometry arrays the core array accounts for only ≈ (2 / 5.9) or about 34 % of the total number of receivers. The ratio remains the same also if instead an equilateral grid arrangement is used throughout. It appears logical, therefore, to concentrate the receiver design effort on realising a universally applicable, cost-efficient, high performance RF front-end, optimised for receive-only use but at the same time incorporating the fast recovery and overload resistance characteristics required in the core array. This unified front-end design could then be used throughout the system, so achieving major synergy effects (reducing the HW/SW development effort, reducing spare parts inventory, simplifying production and maintenance etc.).

8. Conclusions and recommendations

It is shown in Section 3.1 that the ultimate transverse resolution requirement (150 m at 100-km altitude) can only be met through interferometric means. The 3D active element should therefore have a basic set of outlier receive-only arrays put in place from the beginning, even if the construction of the filled central array must then proceed in stages due to a consequential shortage of funding - it should simply be made as large as the available first-stage funding allows.

It is however logical to aim for an initial central array size of at least 5000 elements, as this would have a power-aperture product equal to that of the EISCAT VHF radar and offer greatly increased performance in almost all other respects. Such a system could profitably take over most of the tasks of the VHF immediately upon commissioning.

The central array should then be expanded as funds become available, up to a target size of ≈ 16000 elements or 343, 49-element cells. Provisions for this expansion (e.g. civil works, access points for power and data etc.) should be designed-in from the beginning.

For the same steering angle limit, an equilateral triangular array configuration is shown to provide a much larger grating-lobe-free solid angle than a square one, while at the same time requiring 12% fewer elements per unit area. The equilateral grid is therefore recommended as the preferred array configuration, both for the central array as well as for the outlier (interferometry) arrays. At an inter-element spacing of 0.70 λ, grating-lobe-free radiation pattern out to almost 40^o zenith angle over the whole (0^o - 360^o) azimuth range is guaranteed.

The strong celestial calibrator source Cas-A will be visible in the array grating-lobe-free field of view for almost 90 % of real-time. Another strong calibrator, Cyg-A, will be visible for about 50 % of real-time. Observing these calibrators through a dedicated beam will enable continuous monitoring of the digital beam pointing system performance and the introduction of adaptive pointing corrections.

An element radiator gain in the order of 7 dBi is required to match this element spacing. This can be provided by e.g. a dipole above an infinite groundplane, or by a short two- or three-element Yagi antenna. Both are electrically broadband and the choice between them is therefore largely based on constructional and operational aspects. When the climatic conditions prevailing in the active element deployment area are taken into account, the Yagi emerges as the favoured alternative.

A short 235-MHz three-element X Yagi design (the so-called “Renkwitz Yagi”) has been simulated in NEC. Providing a gain of 7.11 dBi, a bandwidth of 24 MHz, and only minor sensitivity to snow/ice load, it exceeds the electrical requirements in all respects. Several model antennas have been constructed and evaluated. The results obtained are generally in very good agreement with the simulated performance.

Special attention has been paid to the influence of snow and ice on the feedpoint impedance and band-pass characteristics. Vector network analyser measurements on an ice-covered antenna qualitatively verify that the impedance change and passband shift induced by even quite substantial amounts of ice are relatively minor and thus manageable. It is found that if the antenna dimensions are deliberately optimised for about 237.5 MHz, i.e. 2.5 MHz or 1% above the nominal center frequency, the feed-point reflection coefficient remains below -20

dB over the entire (229 – 241) MHz transmission band even when the antenna elements are covered by up to 2.5 mm thick ice. The Renkwitz Yagi design is therefore proposed as a serious candidate for the element radiator.

At a power level of 600 W per array element, the peak power of the 16000-element array will approach 10 MW, thus vastly exceeding the design target of 2 MW. The RF power amplifiers should be biased for linear class-AB2 operation. This will make the power units capable of accommodating any future developments in radar coding, including the possible use of combined phase and amplitude modulations, without any hardware modifications or changes. It will also permit the dynamical application of aperture tapering and/or randomisation on transmission as required.

The receiver function can either be realised as a distinct subsystem, or it can be integrated with the TX exciter and HPA into a combined RF unit, transceiver style. Since the active element array will only contain about one-third of the total number of receivers in the full five-site 3D system, the distinct subsystem approach is recommended. The receiver design effort can then be concentrated on realising a unified, cost-efficient, high performance RF front-end, optimised for receive-only use but also incorporating the fast recovery and overload resistance characteristics required for use in the active array. Major synergy gains should result.

To reduce construction cost and complexity, a degree of sub-grouping of array elements, with a single equipment container per group housing all electronics subsystems and the radiator elements (Yagis) connected to the container through short runs of low-loss coax cable, shall be employed. This arrangement is acceptable perfomance-wise at 235 MHz mainly for two reasons, 1) the sky noise temperature is always above 100 K, and 2) cable losses are lower than at UHF. Under the boundary condition that cable noise and losses shall not be allowed to reduce the rate of statistics by more than 10 % compared to a hypothetical lossless feed system, even under worst-case conditions, and noting that the equilateral grid structure lends itself naturally to a hierarchical, self-similar grouping scheme in the order 7, 49, 343… elements per group, the 49-element cell is shown to be the obvious choice. This cell size is also very suitable for the interferometry application.

The radar performance analysis in Section 5 demonstrates that the extreme joint time/height resolution requirements laid down in PSD Section 2.12 are quite unrealistic; as shown in Table 5, even a 36000-element array configuration utilising advanced modulation schemes would fail to meet the targets at all altitudes by a factor of (70…920)!

However, if the altitude resolution is relaxed by a factor of (2…10), even a 16000-element system will be in a position to meet the 1-s/10-s time resolution requirement at 150…800 km altitude. As shown in Table 6, the SNR will then exceed 20 % at all altitudes, which already brings the system into the region of diminishing returns. Any substantial improvement in altitude resolution would require significantly longer integration times.

The user community is strongly advised to review its requirements and consider whether incoherent-scatter altitude resolutions better than 1 km are really meaningful and required at altitudes above 150 km, keeping in mind that demands for extreme simultaneous time and height resolution must be bought at very high capital investment and operating cost.

References

1. EISCAT_3D Annex 1 to the Contract, http://e7.eiscat.se/groups/EISCAT_3D_info/Annex 1 to the EU Contract/view

2. EISCAT_3D Design Specification Document, http://e7.eiscat.se/groups/EISCAT_3D_info/P_S_D_7.pdf (2005)

3. Philips / NXP Data Sheet, BLF248 VHF push-pull power MOS transistor, http://www.nxp.com/acrobat_download/datasheets/BLF248_3.pdf (2003)

4. J. Markkanen, A Matlab package for Phased Array Beam Shape Inspection, http://e7.eiscat.se/groups/EISCAT_3D_info/e3dant.pdf (2006)

5. T. Grydeland and C. LaHoz, Fundamentals of radar interferometry: One baseline, http://e7.eiscat.se/groups/EISCAT_3D_info/WP5_Interferometry_Stage2_Report_April06.pdf

6. T. Grydeland and C. LaHoz, EISCAT_3D_Radar_Imaging_Arrays_Configurations_Report, http://e7.eiscat.se/groups/EISCAT_3D_info/D5_1_EISCAT_3D_Radar_Imaging_Arrays_Configurations_Report.pdf

7. P.-S. Kildal, Foundation of Antennas; a Unified Approach, Studentlitteratur, Sweden, ISBN 91-44-01322-1

8. E. Brookner (ed.), Practical Phased-Array Antenna Systems, Artech House, Inc. (1991), ISBN 0-89006-563-2

9. J. W. M. Baars, R. Genzel, I. I. K. Pauliny-Toth and A. Witzel, The Absolute Spectrum of Cas-A; An Accurate Flux Density Scale and a Set of Secondary Calibrators, Astron. Astrophysics 61, 99-106 (1977)

10. C. A. Balanis, Antenna Theory; Analysis and Design, John Wiley & Sons (1982), ISBN 0-471-60352-X

11. T. Renkwitz, M. Sc. thesis: “Analysis and Optimisation of Medium Gain X-Yagi Antennas for the EISCAT 3D 237.5MHz Incoherent Scatter Radar Active Array”, http://e7.eiscat.se/groups/EISCAT_3D_info/MScWorkToralfRenkwitzEISCAT3D (2007)

12. M. Baron, The EISCAT facility, J. Atmos. Terr. Phys., 46, 469-472, 1984.

13. T. Nygren, Introduction to Incoherent Scatter Measurements, University of Oulu, 2004, ISSN 1239-3673, ISBN 951-97489-0-3

14. Fukao, S., T. Sato, T. Tsuda, S. Kato, K. Wakasugi, and T. Makihira (1985), The MU radar with an active phased array system 1. Antenna and power amplifiers, *Radio Sci.*, 20(6), 1155–1168.

15. Advanced Modular Incoherent Scatter Radar Homepage, http://isr.sri.com/iono/amisr/

Institutet för rymdfysik

Swedish Institute of Space Physics

Swedish Institute of Space Physics
Box 812, SE- 981 28 Kiruna, SWEDEN
tel. +46-980-790 00, fax +46-980-790 50, e-post: irf@irf.se

www.irf.se